

# Altermagnetic XMCD in Hematite Distinct from Weak Ferromagnetic Contributions

Y. Ishii,<sup>1,\*</sup> N. Sasabe,<sup>1</sup> and Y. Yamasaki<sup>1,2,3,†</sup>

<sup>1</sup>Center for Basic Research on Materials (CBRM),

National Institute for Materials Science (NIMS), Tsukuba 305-0047, Japan

<sup>2</sup>RIKEN Center for Emergent Matter Science (CEMS), Wako 351-0198, Japan

<sup>3</sup>International Center for Synchrotron Radiation Innovation Smart, Tohoku University, Sendai 980-8577, Japan

Altermagnets are compensated collinear magnets that break time-reversal symmetry without net magnetization, enabling unconventional magneto-optical responses. Here, altermagnetic X-ray magnetic circular dichroism (XMCD) is experimentally demonstrated in hematite  $\alpha$ -Fe<sub>2</sub>O<sub>3</sub>. By employing a symmetry-selective geometry in which the x-ray propagation vector is orthogonal to the Dzyaloshinskii-Moriya-induced weak ferromagnetic moment, we isolate a finite XMCD signal that cannot be attributed to conventional weak ferromagnetism. Moreover, we demonstrate that distinct altermagnetic states characterized by different magnetic symmetries can be reversibly switched through the application of an in-plane external magnetic field. Full-multiplet calculations reveal that the signal originates from an anisotropic magnetic dipole moment realized in the  $2p^53d^6$  excited states, despite the isotropic  $2p^63d^5$  ground state. Our results establish XMCD as a direct probe of excited-state magnetic multipoles and provide a general route for the optical detection of altermagnetic order in compensated magnets.

## Introduction

Altermagnetism, a collinear compensated magnetic phase with anisotropic spin symmetry, has recently emerged as a new frontier in spintronics and condensed matter physics [1, 2]. Distinguished from conventional Néel antiferromagnetism (AFM) and ferromagnetism (FM), altermagnets break time-reversal symmetry without net magnetization, driving spin splitting in momentum space with  $d$ -,  $g$ -, and higher-order wave symmetry [1, 3–6]. These materials exhibit remarkable transport and optical responses, including anomalous Hall and Nernst effects [1, 7–10], as well as unconventional magneto-optical dichroism [11–14]. The essential ingredient is the crystal symmetry that connects opposite spin sublattices by proper rotations rather than simple translations or inversions, leading to momentum-dependent spin splitting even in the absence of net magnetization. The symmetry of the spin splitting directly reflects the underlying crystalline point group and determines the anisotropy of spin-dependent responses.

Recently, it has been theoretically demonstrated that X-ray magnetic circular dichroism (XMCD), defined as the difference in the X-ray absorption spectrum (XAS) between right- and left-circularly polarized light, can acquire a finite signal even in AFMs [15–17]. Although XMCD is traditionally regarded as a probe of net magnetization, it is symmetry-allowed in AFMs when the electronic structure is characterized by the symmetry of a cluster magnetic dipole. X-ray absorption is an intra-atomic excitation process, and therefore, even in an AFM, it probes the magnetic dipole components that are ferriocally ordered at each atomic site. Even when the

spin and orbital magnetic dipole moments are completely compensated, XMCD can detect a ferroic-component anisotropic magnetic dipole (AMD) moment that depends on the anisotropic distribution of the electronic states [15, 18]. The total AMD corresponds to the physical quantity of the magnetic dipole term  $T_z$  operator that appears in the XMCD sum rules and has long been recognized in that context [19, 20]. From a magnetic multipole viewpoint, it can be understood as a spinful magnetic dipole moment  $\hat{\mathbf{m}}'$  arising from the tensor product of the spin and the electric quadrupole moment, expressed as

$$\hat{\mathbf{m}}' = \frac{1}{\sqrt{10}}[3(\hat{\mathbf{r}} \cdot \hat{\boldsymbol{\sigma}})\hat{\mathbf{r}} - \hat{r}^2\hat{\boldsymbol{\sigma}}] \quad (1)$$

with position operator  $\hat{\mathbf{r}}$  and the Pauli matrix  $\hat{\boldsymbol{\sigma}}$  [21, 22]. Hence, the magnetic dipole term  $\mathbf{T}$  in the XMCD sum rules can be expressed as  $\mathbf{T} = \sum_i \langle \psi_i | \hat{\mathbf{m}}' | \psi_i \rangle$ , indicating that it corresponds to the sum of the local magnetic dipole expectation values for each occupied orbital  $\psi_i$ . Since X-ray absorption probes excited states, *i.e.* from  $2p^63d^n$  to  $2p^53d^{n+1}$  at  $L$ -edge XAS for  $3d$  transition metals, XMCD can detect such contributions even if the expectation value of the AMD vanishes in the ground state, provided that an anisotropic electronic configuration is realized in the excited state. For instance, while  $\alpha$ -MnTe has no AMD moment in the ground state due to its isotropic  $3d^5$  state of Mn<sup>2+</sup>, the trigonal crystal field and spin-orbit coupling split the  $e_g^\pi$  manifold into anisotropic electronic states carrying opposite AMD moments, resulting in an oscillatory XMCD line shape characteristic of altermagnetic symmetry [23].

## Altermagnetism in Fe<sub>2</sub>O<sub>3</sub>

Among the candidate altermagnetic materials, hematite ( $\alpha$ -Fe<sub>2</sub>O<sub>3</sub>) stands out as a prototypical  $g$ -wave altermagnet. At room temperature, it crystallizes in

\* Correspondence email address: ISHII.Yuta@nims.go.jp

† Correspondence email address: YAMASAKI.Yuichi@nims.go.jp

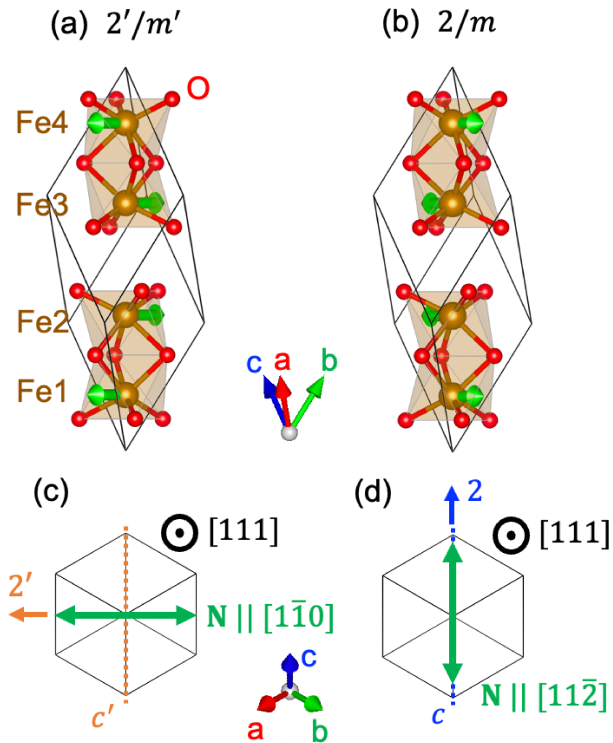


FIG. 1. Crystal and magnetic structure of  $\alpha\text{-Fe}_2\text{O}_3$  for (a) the Néel vector  $\mathbf{N} \parallel [1\bar{1}0]$  and (b)  $\mathbf{N} \parallel [11\bar{2}]$ . The corresponding magnetic point groups are  $2'/m'$  and  $2/m$ , respectively. The structures are visualized using VESTA [24]. Schematic view along the  $[111]$  direction of  $\mathbf{N}$ ,  $c$ - and  $c'$ -glide planes as well as the twofold rotation axes ( $2$  and  $2'$ ) for (c)  $\mathbf{N} \parallel [1\bar{1}0]$  and (d)  $\mathbf{N} \parallel [11\bar{2}]$ , respectively.

the space group of trigonal  $R\bar{3}c$  and exhibits a collinear AFM order. The crystallographic point group is  $\bar{3}m$  (Schoenflies notation  $D_{3d}$ ), characterized by a threefold rotation axis  $[111]_{\text{rh}}$  and a glide plane parallel to it ( $c$ -glide). Note that, throughout this paper, crystallographic directions are expressed in the rhombohedral setting. It is a well-known AFM with a high Néel temperature ( $T_N \sim 950$  K) and undergoes a Morin transition at  $T_M \approx 250$  K; in its high-temperature phase ( $T > T_M$ ), it exhibits a weak ferromagnetic (wFM) moment induced by the Dzyaloshinskii-Moriya (DM) interaction [25, 26]. The Néel vector  $\mathbf{N}$  lies within the  $(111)$  plane. The magnetic symmetry depends on the orientation of  $\mathbf{N}$  relative to the crystallographic mirror planes. When  $\mathbf{N} \parallel \langle 1\bar{1}0 \rangle$ , the magnetic point group (MPG) is  $2'/m'$ ; whereas for  $\mathbf{N} \parallel \langle 11\bar{2} \rangle$ , it becomes  $2/m$ . The distinction arises from whether the relevant mirror operation is preserved as a pure spatial symmetry ( $m$ ) or is combined with time reversal ( $m'$ ). Both MPGs host symmetries of magnetic dipoles. In contrast, below  $T_M$ , when  $\mathbf{N} \parallel [111]$ , MPG becomes  $3/m$ , under which magnetic dipole moments are forbidden.

In the corundum-type crystal structure, local inversion

symmetry between neighboring Fe sites is broken, giving rise to the DM interaction,

$$H_{\text{DM}} = \mathbf{D} \cdot (\mathbf{S}_1 \times \mathbf{S}_2), \quad (2)$$

where  $\mathbf{S}_1$  and  $\mathbf{S}_2$  are neighboring spins, and  $\mathbf{D}$  is the DM vector derived from spin-orbit coupling and exchange interaction in second-order perturbation theory [25, 26]. According to Moriya's symmetry rules [26], the DM vector is constrained to be parallel to the crystallographic threefold axis  $\mathbf{D} \parallel [111]$ . Consequently, the wFM moment induced by the DM interaction is given by  $\mathbf{M}_{\text{wFM}} \propto \mathbf{D} \times \mathbf{N}$ , which lies within the  $(111)$  plane and is perpendicular to both  $\mathbf{N}$  and  $\mathbf{D}$ .

From the viewpoint of magnetic symmetry, the observation of XMCD originating from the AMD is anticipated in  $\alpha\text{-Fe}_2\text{O}_3$ , whose local trigonal crystal field and collinear AFM structure closely resemble those of  $\alpha\text{-MnTe}$  [12, 23, 27]. However, the coexistence of wFM and altermagnetic symmetry makes it experimentally challenging to disentangle the intrinsic AMD-driven XMCD contribution from the conventional wFM-induced signal [28]. Altermagnetic XMCD has recently been reported in Ti-doped  $\alpha\text{-Fe}_2\text{O}_3$  thin-film [14]. In addition, recent theoretical works have predicted that the XMCD signal associated with altermagnetism appears along a direction distinct from that of  $\mathbf{M}_{\text{wFM}}$  [29], while symmetry-driven magneto-optical Kerr effects (MOKE) have also been proposed and experimentally explored [30, 31]. These studies establish that altermagnetic optical responses are symmetry-allowed and potentially observable in  $\alpha\text{-Fe}_2\text{O}_3$ .

For a further decisive experimental identification, a quantitative comparison between measured XMCD spectra and multiplet calculations, together with a systematic investigation of their magnetic-field dependence, is essential to unambiguously separate the altermagnetic contribution from the wFM component. Moreover, since the altermagnetic dipole is expected to be sensitive to epitaxial strain, it is crucial to verify whether altermagnetic XMCD persists in bulk samples, where such strain effects are minimized. In this study, we investigate the XMCD response of bulk  $\alpha\text{-Fe}_2\text{O}_3$  and provide direct evidence for an altermagnetic contribution distinct from the wFM component, supported by symmetry analysis and microscopic multiplet calculations.

## Experimental and Calculation Methods

X-ray magnetic circular dichroism (XMCD) measurements around the Fe  $L_{2,3}$  edges ( $2p \rightarrow 3d$ ) were performed at undulator beamline BL-16A of the Photon Factory (KEK, Japan), using an XMCD end-station equipped with a 5 T superconducting magnet. The spectra were recorded in total electron yield (TEY) mode. The sample is a natural  $\alpha\text{-Fe}_2\text{O}_3$  single-crystal substrate with the  $(111)$  surface orientation, purchased from SurfaceNet GmbH (Germany). The external magnetic field

( $\mathbf{H}_{\text{ext}}$ ) is applied parallel to the X-ray incident direction  $\mathbf{k}$ . The experimental setup is equipped with a motorized single-axis rotation stage. The sample was mounted such that the  $[1\bar{1}2]$  direction is parallel to the rotation axis. At  $\theta = 0^\circ$ ,  $\mathbf{H}_{\text{ext}}$  is applied along the  $[111]$  direction, whereas at  $\theta = 90^\circ$ , the field is approximately directed toward the  $[1\bar{1}0]$  axis. To enhance measurement sensitivity and suppress systematic drifts, the helicity of the circularly polarized X-rays was switched between left and right polarization at a frequency of 10 Hz. The XMCD signal was detected using a lock-in amplifier synchronized to the polarization switching frequency, enabling high-precision extraction of the dichroic signal. All spectra were measured at room temperature.

To interpret the experimental spectra, theoretical spectrum calculations are carried out using the EDRIXS code [32]. The crystal-field parameters are determined from the actual crystal structure based on the CIF obtained from the Materials Project database (mp-19770, primitive cell) [33, 34]. The spectra are obtained by exact diagonalization of the full multiplet Hamiltonian for the  $2p^63d^5$  ground and  $2p^53d^6$  excited states, incorporating intra-atomic Coulomb interactions, spin-orbit coupling ( $\lambda_v = 59$  meV) of valence shells, and the crystal-field effects. The calculated  $3d^5$  ground state follows Hund's rule, resulting in a high-spin state of  $(t_{2g\uparrow})^3(e_{g\uparrow})^2$ . To simulate the AFM ground state at room temperature, an internal magnetic field is introduced into the calculation. The AFM configuration is realized by applying an effective internal field of  $B_{\text{int}} = 50$  meV with corresponding directions and signs on the four Fe sublattices, thereby reproducing the spin polarization consistent with the experimental conditions.

### XMCD Spectra and Magnetic Domain Control

Figure 2(a) shows the XAS and XMCD spectra around the Fe  $L_{2,3}$  edges of  $\alpha\text{-Fe}_2\text{O}_3(111)$ . The upper panel presents the polarization-averaged XAS spectrum  $(I_+ + I_-)/2$ , reflecting the unoccupied Fe  $3d$  density of states under crystal-field and multiplet effects. Here,  $I_{\pm}$  indicates XAS intensity measured with right or left circular polarization. Characteristic multiplet structures corresponding to the high-spin  $\text{Fe}^{3+}$  ( $3d^5$ ) configuration are clearly observed at the  $L_3$  ( $\sim 709$  eV) and  $L_2$  ( $\sim 722$  eV) edges. The lower panel shows the XMCD spectrum defined as  $I_+ - I_-$ , exhibiting the characteristic oscillatory structure typical of altermagnets, which is distinctly different from the conventional XMCD line shape observed in ferromagnets [35]. In addition, the magnitude of this signal is markedly greater than that reported for other altermagnetic systems [11, 12]. Prior to measurement,  $\mathbf{H}_{\text{pre}} = \pm 5$  T was applied along the  $[1\bar{1}0]$  direction to align AFM domains. The spectra were then recorded at zero magnetic field with  $\mathbf{k} \parallel [111]$ . Reversing the sign of the preparatory magnetic field reverses the zero-field XMCD signal, demonstrating that the AFM domains are

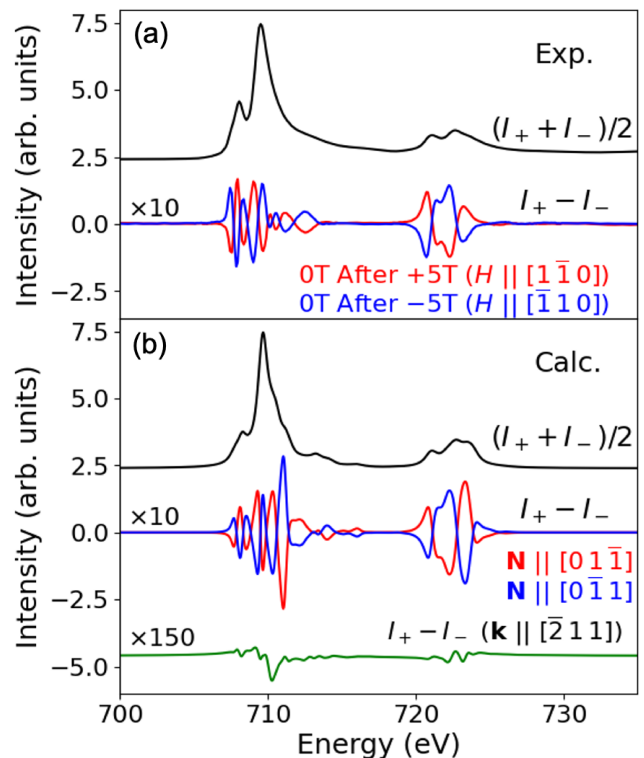


FIG. 2. (a) X-ray absorption spectroscopy (XAS) and X-ray magnetic circular dichroism (XMCD) spectra at the Fe  $L_{2,3}$  edges for  $\alpha\text{-Fe}_2\text{O}_3(111)$ . The upper panel shows the polarization-averaged XAS spectrum,  $(I_+ + I_-)/2$ , measured in total electron yield (TEY) mode. The lower panel displays the XMCD signal, defined as  $I_+ - I_-$ , obtained at 0 T after applying external magnetic fields of  $\pm 5$  T applied along the  $[1\bar{1}0]$  direction. The red and blue curves correspond to measurements after applying  $+5$  T and  $-5$  T, respectively. The XMCD intensity is magnified by a factor of 10 for clarity. (b) Calculated XAS and XMCD spectra. Red and blue lines correspond to XMCD of  $\mathbf{N} \parallel [01\bar{1}]$  and  $\mathbf{N} \parallel [0\bar{1}1]$ . Green line presents XMCD spectrum calculation originating from  $\mathbf{M}_{\text{wFM}}$  along the  $[\bar{2}11]$  direction. The intensity is magnified by a factor of 150.

controllably selected by the pre-applied field.

Since the DM-induced wFM moment lies within the  $(111)$  plane and is perpendicular to  $\mathbf{N}$ , an in-plane magnetic field  $\mathbf{H}_{\text{pre}} \parallel [1\bar{1}0]$  is expected to preferentially select domains with  $2/m$  symmetry ( $\mathbf{N} \parallel [11\bar{2}]$ ), as shown in Fig. 1(d). However, in this symmetry, the magnetic dipole component along  $\mathbf{k} \parallel [111]$  is forbidden, and XMCD should vanish. In contrast, for the  $2'/m'$  configuration, the magnetic dipole can possess a finite projection along the  $[111]$  direction, making XMCD symmetry-allowed. Therefore, the presence of XMCD implies that the AFM ground state under zero field belongs to the  $2'/m'$  MPG.

Under applied  $\mathbf{H}_{\text{pre}} \parallel [1\bar{1}0]$ , the Néel vector belonging to the  $2'/m'$  magnetic point group can, in principle, take either  $\mathbf{N} \parallel [01\bar{1}]$  or  $\mathbf{N} \parallel [10\bar{1}]$ , since these two

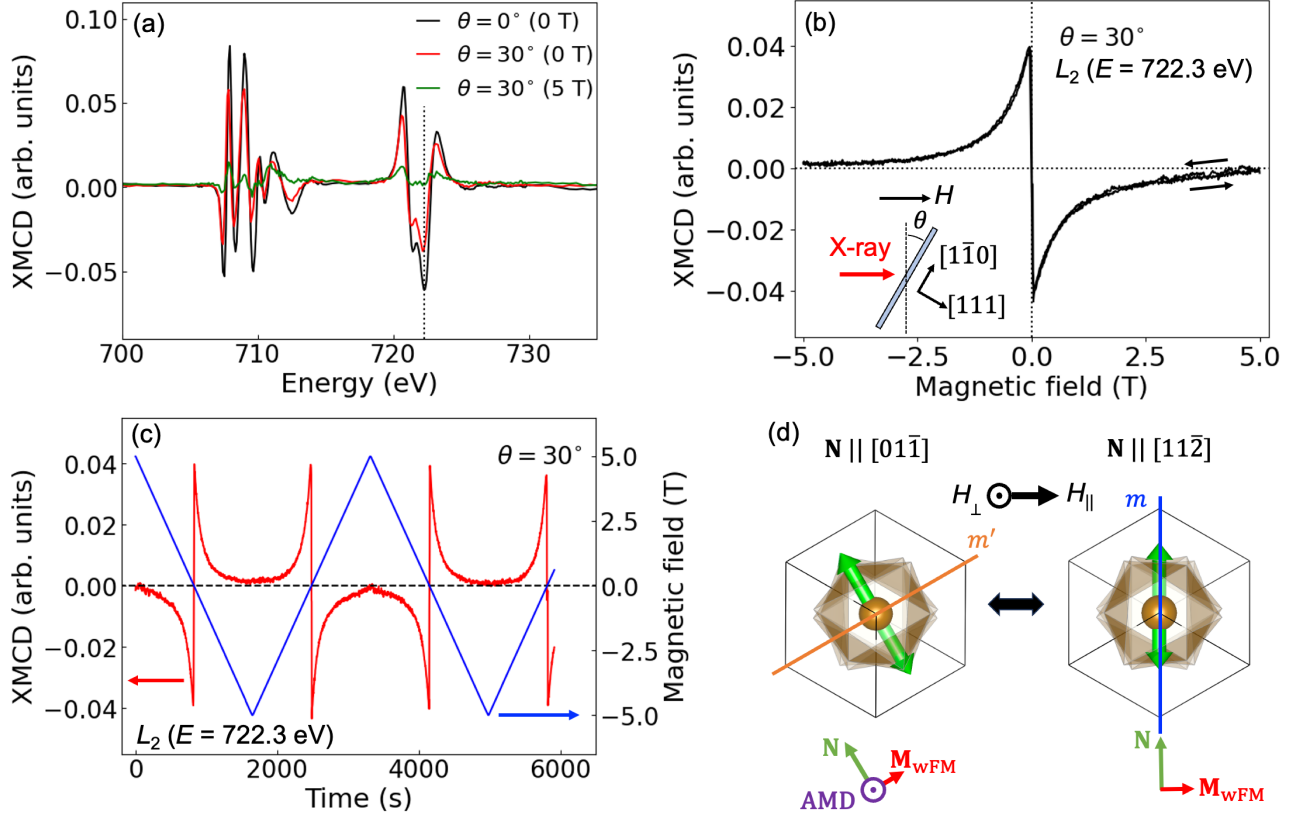


FIG. 3. (a) XMCD spectra measured around Fe  $L_{2,3}$ -edges under external magnetic field.  $\theta$  denotes the tilt angle of the sample respect to the direction of magnetic field and incident X-rays. A dashed vertical line marks  $E = 722.3$  eV. (b) Magnetic-field dependence of the XMCD intensity at  $L_2$  edge ( $E = 722.3$  eV) and  $\theta = 30^\circ$ . The inset illustrates experimental geometry. (c) Time evolution of the XMCD signal at 722.3 eV under a linearly varying magnetic field. (d) Schematic illustration of magnetic structure variation between  $\mathbf{N} \parallel [01\bar{1}]$  and  $\mathbf{N} \parallel [11\bar{2}]$  in the presence of an in-plane  $H_{\parallel} \parallel [1\bar{1}0]$  and out-of-plane  $H_{\perp} \parallel [111]$  magnetic field.

configurations form equal angles with the applied field and are therefore energetically degenerate in the ideal geometry. However, in the actual experiment, a slight misalignment of the sample inevitably introduces a small deviation of  $\mathbf{H}_{\text{pre}}$  from the exact  $[1\bar{1}0]$  direction. Such a minute symmetry-breaking field component lifts the degeneracy between the two domain states and preferentially selects one of the two possible  $\mathbf{N}$  orientations. The XMCD signal retains its sign even after the magnetic field is removed. This persistence of the dichroic response at 0 T indicates that the selected AFM domain remains stable in zero field, demonstrating that  $\mathbf{N}$  orientation is isothermally determined by  $\mathbf{H}_{\text{pre}}$  and preserved as a remanent AFM domain state.

### Comparison with Theoretical Calculations

The spectral line shape and experimental configuration of the observed XMCD ( $\mathbf{k} \perp \mathbf{M}_{\text{wFM}}$ ) differ markedly from that expected from a net wFM moment, indicating a nontrivial origin rooted in crystal symmetry, espe-

cially the local distortion of the ligand field. A closer look at the crystal structure reveals that  $\text{FeO}_6$  octahedra are trigonally distorted and share faces, resembling the NiAs-type structure of  $\alpha$ -MnTe. Recent theoretical studies have revealed that the origin of XMCD in the collinear antiferromagnetic state of  $\alpha$ -MnTe arises from the AMD moment [23]. In the  $\alpha$ - $\text{Fe}_2\text{O}_3$  system addressed in this work, a similar electronic configuration is expected to be realized. To clarify this point, we calculated the XAS spectra based on the electronic states obtained by exact diagonalization of the Hamiltonian, incorporating a crystal field that reflects the actual ligand positions, as well as spin-orbit coupling (SOC) and Coulomb interactions.

The calculation reveals that the AMD moments of the excited state contribute to XMCD for  $\mathbf{k} \parallel [111]$  as well as  $\alpha$ -MnTe [23]. Figure 2(b) shows the calculated XAS and XMCD spectra at the Fe- $L_{2,3}$  edges. The overall undulating spectral shape at both the  $L_3$  and  $L_2$  edges is well reproduced by the calculation in which the XMCD originates from the AMD moment in the excited state. Since AMD contributions have alternating signs, the resulting XMCD exhibits the pronounced oscillatory struc-

ture that is characteristic of altermagnetic XMCD. Beyond reproducing the spectral line shape, the calculation quantitatively accounts for the XMCD intensity relative to the XAS. The remaining discrepancy near the higher-energy shoulder of the main peak may partly originate from the energy dependence of the relaxation time within the multiplet manifold or from Fe off-centering and hybridization with odd-parity orbitals such as the  $4p$  orbital state.

In contrast, the XMCD spectrum for  $\mathbf{k}||[\bar{2}11]$  calculated from the wFM component  $\mathbf{N}||[0\bar{1}1]$  is shown in Fig. 2(b). In the calculation, the canting angle  $0.0554^\circ$  [36] is used to estimate the magnitude of  $\mathbf{M}_{\text{wFM}}$ , and the corresponding XMCD response with  $\mathbf{k}||\mathbf{M}_{\text{wFM}}$  is evaluated within the same multiplet framework. In particular, the characteristic peak structure does not reproduce the experimental features, and the overall magnitude of the calculated signal is more than one order of magnitude smaller than the observed XMCD intensity. These results demonstrate that the experimentally observed XMCD cannot be attributed to the DM-induced wFM moment.

### Magnetic field dependence

Figure 3(a) and (b) show the  $\mathbf{H}_{\text{ext}}$  dependence of XMCD measurements taken with the sample tilted such that  $\mathbf{H}_{\text{ext}}$  and  $\mathbf{k}$  are oriented  $30^\circ$  away from the surface normal. By rotating the sample around the  $[11\bar{2}]$  axis, the magnetic field acquires an in-plane component along the  $[1\bar{1}0]$  direction, as shown in the inset of Fig. 3(b). The difference in the XMCD intensity between  $\theta = 0^\circ$  and  $\theta = 30^\circ$  at 0 T originates from the change in the experimental geometry. While the spectral line shape is essentially unchanged, the XMCD intensity is suppressed by the applied magnetic field, indicating that the magnetic field-induced modification of the underlying magnetic configuration occurs rather than a simple enhancement of a wFM contribution. Figure 3(b) displays the magnetic-field dependence of the XMCD intensity at the  $L_2$  edge ( $E = 722.3$  eV) for  $\theta = 30^\circ$ . The signal exhibits a sharp sign reversal across zero field and gradual suppression with a characteristic antisymmetric profile. This behavior is inconsistent with a conventional ferromagnetic hysteresis loop and instead suggests that the XMCD originates from a field-selectable antiferromagnetic order parameter.

The dynamic response is further demonstrated in Fig. 3(c), where the magnetic field is linearly swept over time. The XMCD signal follows the field variation reproducibly and switches sign whenever the field polarity changes, confirming that the observed dichroism is directly coupled to the field-controlled magnetic domain state. As illustrated in Fig. 3(d),  $\mathbf{N}||[11\bar{2}]$  should be stabilized rather than  $\mathbf{N}||[10\bar{1}]$  (or  $[01\bar{1}]$ ) under an applied magnetic field  $\mathbf{H}||[1\bar{1}0]$ . Therefore, the suppression of XMCD indicates a field-induced spin reorientation

from the  $2'/m'$  to the  $2/m$  state. When the magnetic field is reduced back to zero, the XMCD signal recovers, confirming that the  $2'/m'$  magnetic structure is the stable configuration in zero field. Such a magnetic-field response further supports the interpretation that the observed XMCD originates from the AMD in  $2'/m'$  state rather than from the wFM.

## Discussion

### Electronic State

The microscopic origin of the XMCD signal is investigated in the collinear AFM state in the corundum structure. The five degenerate  $d$ -orbitals of the Fe ion split into  $e_g$  and  $t_{2g}$  states due to the octahedral crystal field ( $O_h$ ). A trigonal distortion reduces the symmetry to  $D_{3h}$  and causes these degenerated states to split further: the  $t_{2g}$  level splits into  $a_{1g}$  and  $e_g^\pi$  components. Using the spherical harmonic basis  $|m\rangle$ , the  $a_{1g}$  is represented by  $|0\rangle$ , and the  $e_g^\pi$  states are  $|\pi_\pm\rangle = \cos\zeta|\pm 2\rangle \mp \eta_j \sin\zeta|\mp 1\rangle$  with  $\zeta$  depending on the trigonal distortion. The four inequivalent Fe sites are distinguished by the parameter  $\eta_j$  at the  $j$ -th site, taking the values  $\eta_1 = \eta_4 = 1$  and  $\eta_2 = \eta_3 = -1$ . In the actual crystal structure, the Fe atomic positions are slightly displaced, and the oxygen octahedra are twisted around the  $[111]$  axis, leading to a further reduction in symmetry.

Figure 4 illustrates the spatial distribution of the electronic states, calculated by the exact diagonalization of the single-ion Hamiltonian, and the expectation value of the AMD moment, *i.e.* the  $m'_z$  operator in Eq. (1). When  $\mathbf{N} || [111]$ , the magnetic structure does not break the threefold rotational symmetry of the crystal; thus, the electronic states retain trigonal symmetry, preserving the  $e_g^\pi$  and  $a_{1g}$  manifolds, as shown in Fig. 4(a). In this situation, the local AMD becomes parallel or antiparallel to the spin moment, leading to complete cancellation. In contrast, when  $\mathbf{N} || [11\bar{2}]$  or  $\mathbf{N} || [1\bar{1}0]$ , the magnetic structure breaks the threefold rotational symmetry of the crystal. As a consequence, the  $e_g^\pi$  manifold is further modulated by spin-orbit coupling, giving rise to electronic states  $\psi_a$  and  $\psi_b$ , which produce a more anisotropic electronic distribution, as shown in Fig. 4(b) and 4(c). For  $\mathbf{N} || [1\bar{1}0]$ , the states  $\psi_a$  and  $\psi_b$  exhibit finite AMD components along the  $[111]$  axis. The AMD components at the two Fe sites possess identical projections along  $[111]$ , leading to ferroic alignment of the AMD. However, for  $\mathbf{N} || [11\bar{2}]$ , the local AMD components at the Fe1 and Fe2 sites are symmetry-opposed and cancel each other, yielding no net projection along the  $[111]$  direction. These results establish a direct correspondence between the MPG symmetry and the electronic structure.

It should be noted that such an AMD does not emerge from an isotropic electronic state. For example, in the case of  $t_{2g}$  orbitals, the expectation value of  $t_z$  cancels

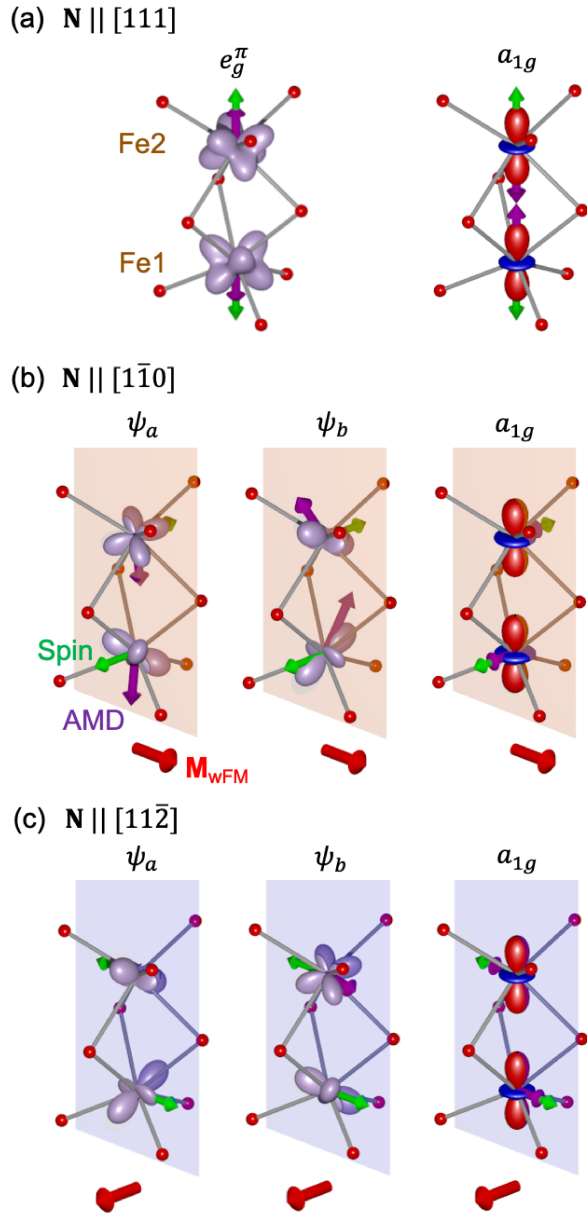


FIG. 4. Spin and orbital configurations at two lower Fe sites for (a)  $\mathbf{N} \parallel [111]$ , (b)  $\mathbf{N} \parallel [1\bar{1}0]$ , (c)  $\mathbf{N} \parallel [11\bar{2}]$ . Red, blue, and purple lobes represent orbitals of  $\psi_{a,b}$ ,  $e_g^\pi$ , and  $a_{1g}$  electronic states. Green, purple, and red arrows denote antiferromagnetic spin, AMD, and ferromagnetic spin moments ( $\mathbf{M}_{\text{wFM}}$ ), respectively. Red and blue boards indicate  $c'$ -glide and  $c$ -glide planes, respectively.

out when summed over the three orbitals. In  $\text{Fe}_2\text{O}_3$ ,  $\text{Fe}^{3+}$  has a high-spin  $3d^5$  electronic configuration,  $|\psi_{\text{gs}}\rangle = |(t_{2g}^\uparrow)^3(e_g^\uparrow)^2\rangle$ , which is isotropic; therefore, the  $T_z$  terms vanish in the ground state  $\langle\psi_{\text{gs}}|T_z|\psi_{\text{gs}}\rangle = 0$ . However, upon excitation from the core level, the system reaches  $2p^53d^6$  configurations, where the minority-spin states split into distinct energy eigenstates,  $\psi_a$ ,  $\psi_b$ , and

$a_{1g}$ . For each excitation energy, the total transition probability is obtained by summing over all possible core-hole configurations, and the XMCD signal emerges from the difference between left- and right-circularly polarized absorption, which is proportional to the AMD moment [22]. In practice, the spectral shape is further modulated by the Coulomb interaction between the  $3d$  electrons and the core hole, resulting in a more complex lineshape, as shown in Fig. 2(a). In any case, even if the AMD vanishes in the ground state, X-ray absorption reflects the properties of the excited states; hence, XMCD originating from AMD is symmetry-allowed.

#### *Dzyaloshinskii–Moriya vector configuration*

Importantly, the observed XMCD in  $\alpha\text{-Fe}_2\text{O}_3$  appears along a direction orthogonal to the DM-induced wFM moment. As shown in Fig. 2(b), the XMCD expected solely from the wFM component is more than an order of magnitude smaller than the measured signal, excluding the wFM as its primary origin. Instead, the XMCD arises from the AMD contribution in the excited state. This behavior sharply contrasts with previously studied non-collinear AFM and altermagnetic systems with magnetic dipole symmetry, such as  $\text{Mn}_3\text{Sn}$  and  $\alpha\text{-MnTe}$ , where the wFM and AMD axial vectors are symmetry-parallel, making their experimental separation difficult [12, 16, 27]. Hematite thus provides a rare example in which the AMD-induced XMCD is symmetry-orthogonal to the ground-state wFM moment. This orthogonality directly demonstrates that in-plane axial-vector degrees of freedom remain active in the  $2'/m'$  MPG, and that the excited-state AMD and ground-state wFM originate from distinct symmetry channels.

From symmetry considerations, the contrast can be understood by comparing DM vectors based on Moriya's rule [26], in which the direction of the DM vector is constrained by the local symmetry at the midpoint between two magnetic ions. In the present case, the midpoint between site 1 and site 2 possesses a threefold axis ( $R_3 \parallel [111]$ ) and a twofold axis ( $R_2 \parallel (1\bar{1}0)$ ), requiring the DM vector to be parallel to the  $R_3$  axis and perpendicular to the  $R_2$  axis. These symmetry constraints uniquely fix the DM vector along the  $[111]$  direction, as shown in Figs. 5(a) and 5(b). We denote this purely crystallographic contribution between site  $i$  and site  $j$  as  $\mathbf{D}_c^{ij}$ . Since an inversion center exists at the midpoint between site 2 and site 3, one obtains  $\mathbf{D}_c^{23} = 0$ , and by symmetry  $\mathbf{D}_c^{34} = -\mathbf{D}_c^{12}$ . As a consequence, the resulting wFM moment is necessarily confined within the plane perpendicular to  $[111]$ .

However, when the Néel vector lies within the  $(111)$  plane, magnetostriction can induce a lattice distortion that breaks the  $R_3$  symmetry, leaving only the  $R_2$  axis. Under this reduced symmetry, the DM vector is no longer strictly constrained to the  $[111]$  direction and can tilt away from it, as shown in Fig. 5(c). We denote the

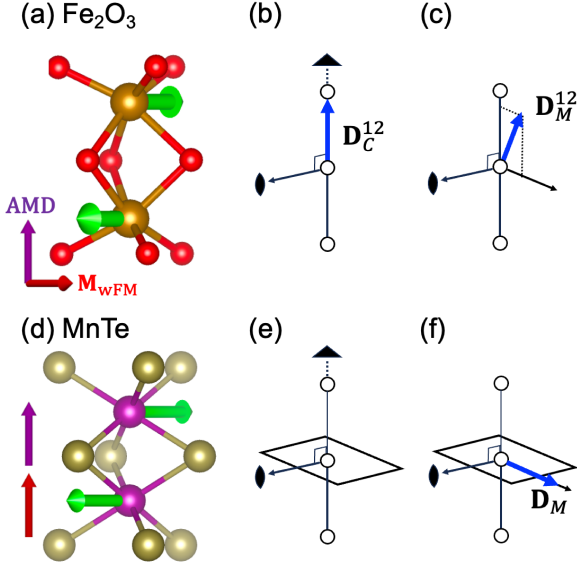


FIG. 5. Comparison of the weak ferromagnetic dipole, the anisotropic magnetic dipole, and the DM vector in (a)  $\alpha\text{-Fe}_2\text{O}_3$  and (d)  $\alpha\text{-MnTe}$ . (b) In the cluster of site 1 and 2 in  $\alpha\text{-Fe}_2\text{O}_3$ , the DM vector  $\mathbf{D}_C^{12}$  associated with the Fe-O-Fe bonds aligns parallel to the 3-fold rotational axis and perpendicular to the 2-fold axis of crystal structure. (c) Under magnetoelastic distortion, the crystal symmetry is slightly lowered, leading to a small tilt of the DM vector  $\mathbf{D}_M^{12}$  away from the ideal symmetry axis. (e) In MnTe-type systems, in addition to the 3- and 2-fold rotational axis, the mirror symmetry perpendicular to the 3-fold axis makes  $\mathbf{D}_C = 0$ . (f) When magnetoelastic distortion lowers the symmetry, the constraint is lifted and a finite DM vector  $\mathbf{D}_M$  emerges, oriented perpendicular to the original 3-fold and 2-fold rotational axes.

magnetostriction-modified DM vector as  $\mathbf{D}_M^{12}$ . Since it acquires a component perpendicular to  $[111]$  and  $\mathbf{D}_M^{34} = -\mathbf{D}_M^{12}$  due to inversion symmetry, it can, in principle, generate a wFM moment along the  $[111]$  axis. However, since the  $3d^5$  ground state has no orbital degree of freedom in practice, the magnetostriction effect is expected to be weak; therefore,  $\mathbf{D}_M$  and  $\mathbf{D}_C$  are assumed to be nearly parallel ( $\mathbf{D}_M^{12} \sim \mathbf{D}_C^{12}$ ). This symmetry reduction is analogous to the emergence of wFM in  $\alpha\text{-MnTe}$ , where the midpoint between magnetic ions possesses not only the  $R_3$  axis but also a mirror plane perpendicular to it ( $M_\perp$ ) as shown in Figs. 5(d) and 5(e). According to Moriya's rules, these symmetry elements prohibit the DM interaction, yielding  $\mathbf{D}_C = 0$  in the high-symmetry phase [26]. However, once magnetic ordering sets in, the  $R_3$  symmetry is broken while the  $R_2$  axis remains. Under this reduced symmetry,  $\mathbf{D}_M$  is constrained to be perpendicular to the  $R_2$  axis and to lie within  $M_\perp$ , which forces it to orient completely perpendicular to the original  $R_3$  axis, as shown in Fig. 5(f). As a result, a small but finite ferromagnetic moment emerges along the  $R_3$  axis [37].

Overall, in MnTe, the DM interaction emerges only

after the reduction of crystal symmetry induced by magnetic ordering. In contrast, in  $\alpha\text{-Fe}_2\text{O}_3$ , the DM interaction component  $\mathbf{D}_C$ , which is already allowed by the original crystallographic symmetry, serves as the primary origin of wFM. This difference is reflected in the distinct directions along which the wFM moment appears in the two systems. From the viewpoint of electronic structure, however, the underlying mechanism of XMCD is common to both materials. In each case, the  $R_3$  symmetry is broken by magnetic ordering, and spin-orbit coupling induces an anisotropic electronic charge distribution, such as in  $e_g^\pi$  orbital. As a consequence, the AMD component is aligned along the  $[111]$  axis, giving rise to a finite XMCD signal for  $\mathbf{k} \parallel [111]$  [23]. Therefore, while the microscopic origin of XMCD is essentially the same in both systems, the presence or absence of  $M_\perp$  determines the direction along which  $\mathbf{M}_{\text{wFM}}$  develops.

## Conclusion

In conclusion, we have experimentally demonstrated the altermagnetic XMCD response in  $\alpha\text{-Fe}_2\text{O}_3$  at room temperature. By employing a specific experimental geometry with  $\mathbf{k} \parallel [111]$  and  $\mathbf{k} \perp \mathbf{M}_{\text{wFM}}$ , we successfully isolated the symmetry-allowed XMCD signal originating from the  $2'/m'$  magnetic state and excluded the conventional weak-ferromagnetic contribution. The observed oscillatory line shape, characteristic of altermagnetic symmetry, is well reproduced by full-multiplet calculations based on exact diagonalization of the realistic electronic Hamiltonian. Furthermore, reversible switching between different altermagnetic states characterized by the  $2'/m'$  and  $2/m$  MPGs can be achieved through the application of an in-plane external magnetic field.

Importantly,  $\alpha\text{-Fe}_2\text{O}_3$  provides a unique platform in which the AMD-induced XMCD is symmetry-orthogonal to the DM-induced weak ferromagnetic moment. This orthogonality enables a clear experimental separation between intrinsic altermagnetic responses and conventional weak ferromagnetism. Our results establish hematite as a prototypical  $g$ -wave altermagnet with a spinful magnetic dipole symmetry and demonstrate that XMCD serves as a powerful probe of altermagnetic order through excited-state multipole responses. These findings open a robust pathway toward the optical detection and control of altermagnetic states in room-temperature spintronic materials.

## Acknowledgment

The authors are grateful to K. Ozawa and K. Amemiya for their support of the experiments and to T. Arima for insightful discussions. This work was supported supported by JSPS KAKENHI (Grants No. JP19K23590, JP19H04399, JP20K20107, JP23K17145, JP24K03205, JP24H01685, JP25K03387), by PRESTO

(JPMJPR2102) and CREST (JPMJCR1861 and JPMJCR2435) Japan Science and Technology Agency (JST). The synchrotron radiation experiments were per-

formed in the Photon Factory with the approval of the Photon Factory Program Advisory Committee (Proposal No. 2024G615, 2025G630).

- 
- [1] L. Šmejkal, R. Gonzalez-Hernandez, T. Jungwirth, and J. Sinova, *Sci. Adv.* **6**, eaba9399 (2020).
- [2] L. Šmejkal, J. Sinova, and T. Jungwirth, *Phys. Rev. X* **12**, 031042 (2022).
- [3] Y. Noda, K. Ohno, and S. Nakamura, *Phys. Chem. Chem. Phys.* **18**, 13294 (2016).
- [4] T. Okugawa, K. Ohno, Y. Noda, and S. Nakamura, *Journal of Physics: Condensed Matter* **30**, 075502 (2018).
- [5] K.-H. Ahn, A. Hariki, K.-W. Lee, and J. Kuneš, *Phys. Rev. B* **99**, 184432 (2019).
- [6] M. Naka, S. Hayami, H. Kusunose, Y. Yanagi, Y. Motome, and H. Seo, *Nature Communications* **10** (2019).
- [7] R. D. Gonzalez Betancourt, J. Zubáč, R. Gonzalez-Hernandez, K. Geishendorf, Z. Šobáň, G. Springholz, K. Olejník, L. Šmejkal, J. Sinova, T. Jungwirth, S. T. B. Goennenwein, A. Thomas, H. Reichlová, J. Železný, and D. Kriegner, *Phys. Rev. Lett.* **130**, 036702 (2023).
- [8] H. Reichlova, R. Lopes Seeger, R. González-Hernández, I. Kounta, R. Schlitz, D. Kriegner, P. Ritzinger, M. Lammel, M. Leiviskä, A. Birk Hellenes, K. Olejník, V. Petříček, P. Doležal, L. Horak, E. Schmoranzero, A. Badura, S. Bertaina, A. Thomas, V. Baltz, L. Michez, J. Sinova, S. T. B. Goennenwein, T. Jungwirth, and L. Šmejkal, *Nature Communications* **15**, 4961 (2024).
- [9] T. Sato, S. Haddad, I. C. Fulga, F. F. Assaad, and J. van den Brink, *Phys. Rev. Lett.* **133**, 086503 (2024).
- [10] S. Sheoran and P. Dev, *Phys. Rev. B* **111**, 184407 (2025).
- [11] A. Hariki, A. Dal Din, O. J. Amin, T. Yamaguchi, A. Badura, D. Kriegner, K. W. Edmonds, R. P. Campion, P. Wadley, D. Backes, L. S. I. Veiga, S. S. Dhesi, G. Springholz, L. Šmejkal, K. Výborný, T. Jungwirth, and J. Kuneš, *Phys. Rev. Lett.* **132**, 176701 (2024).
- [12] O. J. Amin, A. Dal Din, E. Golias, Y. Niu, A. Zakharov, S. C. Fromage, C. J. B. Fields, S. L. Heywood, R. B. Cousins, F. Maccherozzi, J. Krempaský, J. H. Dil, D. Kriegner, B. Kiraly, R. P. Campion, A. W. Rushforth, K. W. Edmonds, S. S. Dhesi, L. Šmejkal, T. Jungwirth, and P. Wadley, *Nature* **636**, 348 (2024).
- [13] P. Krüger, *Phys. Rev. Lett.* **135**, 196703 (2025).
- [14] E. Galindez-Ruales, R. Gonzalez-Hernandez, C. Schmitt, S. Das, F. Fuhrmann, A. Ross, E. Golias, A. Akashdeep, L. Lünenbürger, E. Baek, W. Yang, L. Šmejkal, V. Krishna, R. Jaeschke-Ubierno, J. Sinova, A. Rothschild, C.-Y. You, G. Jakob, and M. Kläui, *Advanced Materials* **37**, e05019 (2025).
- [15] Y. Yamasaki, H. Nakao, and T.-h. Arima, *Journal of the Physical Society of Japan* **89**, 083703 (2020).
- [16] M. Kimata, N. Sasabe, K. Kurita, Y. Yamasaki, C. Tabata, Y. Yokoyama, Y. Kotani, M. Ikhlas, T. Tomita, K. Amemiya, H. Nojiri, S. Nakatsuji, T. Kogetsune, H. Nakao, T.-h. Arima, and T. Nakamura, *Nat. Commu.* **12**, 5582 (2021).
- [17] N. Sasabe, M. Kimata, and T. Nakamura, *Phys. Rev. Lett.* **126**, 157402 (2021).
- [18] N. Sasabe, M. Mizumaki, T. Uozumi, and Y. Yamasaki, *Physical Review Letters* **131**, 216501 (2023).
- [19] B. T. Thole, P. Carra, F. Sette, and G. van der Laan, *Physical Review Letters* **68**, 1943 (1992).
- [20] P. Carra, B. T. Thole, M. Altarelli, and X. Wang, *Physical Review Letters* **70**, 694 (1993).
- [21] S. Hayami and H. Kusunose, *Journal of the Physical Society of Japan* **93**, 072001 (2024).
- [22] Y. Yamasaki, Y. Ishii, and N. Sasabe, *Science and Technology of Advanced Materials* **26**, 2513217 (2025).
- [23] N. Sasabe, Y. Ishii, and Y. Yamasaki, *Phys. Rev. B* **112**, 224401 (2025).
- [24] K. Momma and F. Izumi, *Journal of Applied Crystallography* **44**, 1272 (2011).
- [25] I. Dzyaloshinskii, *Journal of Physics and Chemistry of Solids* **4**, 241 (1958).
- [26] T. Moriya, *Physical Review* **120**, 91 (1960).
- [27] A. Hariki, K. Sakurai, T. Okauchi, and J. Kuneš, *npj Quantum Materials* **10**, 49 (2025).
- [28] H. Jani, J.-C. Lin, J. Chen, J. Harrison, F. Maccherozzi, J. Schad, S. Prakash, C.-B. Eom, A. Ariando, T. Venkatesan, and P. G. Radaelli, *Nature* **590**, 74–79 (2021).
- [29] R. Xie, H. Zerdoumi, and H. Zhang, “X-ray magnetic circular dichroism of altermagnet  $\alpha$ -Fe<sub>2</sub>O<sub>3</sub> based on multiplet ligand-field theory using wannier orbitals,” (2025), [arXiv:2512.11664 \[cond-mat.mtrl-sci\]](https://arxiv.org/abs/2512.11664).
- [30] J. Luo, X. Zhou, J. Liang, L. Wang, Q. Zhou, Y. Jiang, W. Wang, Y. Yao, L. Yang, and W. Jiang, *Chinese Physics Letters* **43**, 020713 (2026).
- [31] H. Pan, R.-C. Xiao, J. Han, H. Zhu, J. Li, Q. Niu, Y. Gao, and D. Hou, *Physical Review Letters* **136** (2026), [10.1103/q8ym-l2zt](https://arxiv.org/abs/10.1103/q8ym-l2zt).
- [32] Y. Wang, G. Fabbri, M. Dean, and G. Kotliar, *Computer Physics Communications* **243**, 151 (2019).
- [33] A. Jain, S. P. Ong, G. Hautier, *et al.*, *APL Materials* **1**, 011002 (2013).
- [34] M. K. Horton, P. Huck, R. X. Yang, J. M. Munro, S. Dwaraknath, A. M. Ganose, R. S. Kingsbury, M. Wen, J. X. Shen, T. S. Mathis, A. D. Kaplan, K. Berket, J. Riebesell, J. George, A. S. Rosen, E. W. C. Spott-Smith, M. J. McDermott, O. A. Cohen, A. Dunn, M. C. Kuner, G.-M. Rignanese, G. Petretto, D. Waroquiers, S. M. Griffin, J. B. Neaton, D. C. Chrzan, M. Asta, G. Hautier, S. Cholia, G. Ceder, S. P. Ong, A. Jain, and K. A. Persson, *Nature Materials* **24**, 1522–1532 (2025).
- [35] Y. Yamasaki, N. Sasabe, Y. Ishii, Y. Sekiguchi, A. Sumiyoshiya, Y. Tanimoto, Y. Kotani, T. Nakamura, and H. Nomura, *Science and Technology of Advanced Materials: Methods* **5** (2025), [10.1080/27660400.2025.2544528](https://doi.org/10.1080/27660400.2025.2544528).
- [36] A. H. Hill, F. Jiao, P. G. Bruce, A. Harrison, W. Kockelmann, and C. Ritter, *Chemistry of Materials* **20**, 4891 (2008).
- [37] K. P. Kluczyk, K. Gas, M. J. Grzybowski, P. Skupiński, M. A. Borysiewicz, T. Fas, J. Suffczyński, J. Z. Domagała, K. Graszka, A. Mycielski, I. K. H. Baj, K. Výborný, M. Sawicki, and M. Gryglas-Borysiewicz, *Physical Review B* **110**, 155201 (2024).